

Building Supramolecular Chirality in Organic Solar Cells Enables High-Performing Circularly Polarized Light Detection

Lixuan Liu

National Center for Nanoscience and Technology

Yang Yang

National Center for Nanoscience and Technology <https://orcid.org/0000-0001-8912-7240>

Jianqi Zhang

National Center for Nanoscience and Technology <https://orcid.org/0000-0002-3549-1482>

Waqar Memon

National Center for Nanoscience and Technology

Yajie Zhang

National Center for Nanoscience and Technology

Zhixiang Wei (✉ weizx@nanoctr.cn)

National Center for Nanoscience and Technology <https://orcid.org/0000-0001-6188-3634>

Article

Keywords: CPL detectors, chiral optoelectronics, organic solar cells

Posted Date: July 10th, 2020

DOI: <https://doi.org/10.21203/rs.3.rs-39893/v1>

License: © ⓘ This work is licensed under a Creative Commons Attribution 4.0 International License.

[Read Full License](#)

Abstract

High-performing direct circularly polarized light (CPL) detectors are urgently needed for the development of chiral optoelectronics. We herein report the direct CPL detectors based on chiral organic small-molecule donor–fullerene acceptor bulk heterojunction organic solar cells (OSCs). By building supramolecular chirality in active layer of OSCs, the chiral OSC demonstrates its highest short-circuit current dissymmetry factor of 0.17 among state-of-the-art direct CPL detectors possessing intrinsic chirality. It demonstrates a significant difference in responsivity of 40 mA W^{-1} upon opposite CPL illumination, four times higher than that of the best reported chiral perovskite CPL detectors to date. The association between the device metrics crucially relating to CPL detection and the anisotropic factor (g -factor) of the active layers revealed that supramolecular chirality is vital to the CPL detectability of OSCs. Given unique but ubiquitous observed supramolecular chirality induction and transfer in organic conjugated systems, highly sensitive CPL detectors based on chiral OSCs show great potential for promoting the development of practical direct CPL detection.

Introduction

Polarization is one of the most important properties of light. When the electric field vector of a light beam propagates along the alternative clockwise or counterclockwise helical trajectory, it can be defined as right- or left-handed circularly polarized light (r- or l-CPL), accordingly. Although the human visual system is insensitive to the handedness of CPL, some creatures, such as beetles, crabs, cuttlefish and mantis shrimp take advantage of unique interactions between their intrinsic chiral tissues or structures and the polarization states of CPL for camouflage¹, visual contrast, communication, bioinformation transfer and navigation^{2–4}. The unique polarization state enables CPL to be applied to some cutting-edge science and technology breakthroughs, such as drug screening⁵, quantum optics^{6,7}, optical communications⁷ and imaging^{8–10}. An intriguing topic closely associated with these issues is the sensitive discrimination of opposite handedness between l- and r-CPL by electronic devices^{11–18}. However, the realization of CPL detection in inorganic photodetectors excessively relies on packaged filters consisting of quarter-wave plates and linear polarizers because of the inherent achiral property of inorganic semiconductors. This feature consequently impedes the simplification and miniaturization of photodetectors for further integration in conventional electronic equipment^{19,20}.

As such, direct CPL detection has greatly progressed by using electronic devices based on active materials with intrinsic chirality. These materials include organic conjugated small molecules and polymers^{11,12,16,21}, hybrid organic–inorganic perovskite materials^{14,15,18} and plasmonic metamaterials^{22,23}. Among these materials, the potential of organic conjugated molecules has attracted great attentions in promoting the advancement of chiral optoelectronics, including efficient CPL detection and beyond. Single-handed intermolecular aggregations from organic conjugated molecules result in the remarkable enhancement in anisotropic factor (g -factor) under unique characters in supramolecular chirality induction, transfer and amplification^{24,25}. Circular dichroism (CD) represents the difference

between the absorptions of l- and r-CPL resulted from the molecular and supramolecular chirality of samples, which originate from the electronic transitions of the chromophore and provide detailed information on chiral interaction^{26,27}. Whereas the *g*-factor is derived from but quantifies the CD intensity thus it is in favor of the lateral comparison of CD intensity among the samples²⁷. The enhanced *g*-factor in organic semiconductors indicates an intensified predominant absorption in r- or l-CPL at certain wavelengths, which are vital to the distinct disparity of photoinduced charge carrier densities in photodetectors. This feature immensely caters for the demands for sensitive CPL detection.

Organic solar cells (OSCs) acquire photocurrent via charge transportation and collection after exciton separation upon photoexcitation in active blends consisting of an electron-donating material and an electron-accepting material. Bulk heterojunctions (BHJs) formed in the blends via phase separation between the donor and acceptor from their mixed solutions. As bicontinuous donor and acceptor phases are in favor of the corresponding hole and electron transport and affluent interface is beneficial to the photo-induced exciton separation with a high efficiency, BHJs are recognized as kernel for an efficient photoelectric conversion²⁸. Massive organic conjugated semiconductors have been constantly developed for OSCs considered as one of the most promising next-generation energy conversion devices for sustainable clean energy. The structure–function relationship between the aggregation morphologies of the active blends and photovoltaic performance of OSCs has been well established. OSCs are also powerful platforms for optoelectronic detection, particularly as CPL detection diodes^{16,21}; however, this feature is a promising area that is still under development^{29–32}. OSCs with small molecule as a donor and fullerene as an acceptor were extensively studied with well-defined charge carrier transport and photogeneration on account of appropriate phase separation. Donors possess conjugated chromophores, so they are the predominant counterpart responsible for light absorption in such systems. The appropriate phase separation with a high purity in the active blends enables minimal optical property perturbation, which in turn, elects OSCs to act as one of the most potential candidates for CPL detection.

On this basis, we fabricated BHJ OSCs by selecting chiral diketopyrrolopyrrole – hexathiophene (DPP6T) as a donor and (6,6)-phenyl C₆₁ butyric acid methyl ester (PC₆₁BM) as an acceptor (Fig. 1a).

Supramolecular chirality was built in OSCs via the single-handed assemblies of donors. The chiral OSCs exhibit a specific detection scenario analogous to the Cotton effect of their chiral donor phases. In the quantified study of the *g*-factor and CPL detection sensitivity of OSCs, an increase in chiral centers of the donor endowed active blends with drastically enhanced *g*-factor, which in turn produced chiral OSCs to detect CPL accurately. The explicit selective CPL absorption with expanded wavelengths resulted from progressive chirality induction and transfer can be generally observed in organic semiconductors. Our strategy is likely to manifest the potential of chiral OSCs in promoting the development of direct CPL detection.

Results

Building supramolecular chirality in OSCs We synthesized two pairs of chiral donors for OSCs by modifying the DPP6T chromophore with enantiomeric side chains, namely, (s)- or (R)-2,6-dimethyloctane (Fig. 1b). The DPP chromophore was selected because of its recognized light absorption efficiency and charge carrier properties^{33,34}. These chiral molecules are abbreviated as (s,s,s,s)-DPP6T, (s,s)-DPP6T, (R,R,R,R)-DPP6T, and (R,R)-DPP6T based on whether enantiomeric (s)- or (R)-2,6-dimethyloctane is attached. The electrochemical energy levels of these chiral molecules were measured by cyclic voltammetry (CV) method (Supplementary Fig. 1a). The highest and lowest occupied molecular orbits of these chiral donors matched well with the molecular energy level of the PC₆₁BM acceptor (Supplementary Fig. 1b).

CD and ultraviolet–visible (UV–vis) spectrums were combined to study the molecular and supramolecular chirality in solutions and spin-coating films of neat DPP6T donors and their corresponding blends with PC₆₁BM acceptors (Fig. 1c, d, e and f). The absorptions of all these chiral DPP6T donors in the solution were almost identical in the UV–vis regions (dash lines in Fig. 1c and Supplementary Fig. 2). The absorption peaks at ca. 640 and 600 nm could be ascribed to the 0–0 and 0–1 vibration bands of the intramolecular charge transfer (ICT) between the DPP-accepting unit and thiophene donor moieties; the peaks at ca. 380 nm were due to intramolecular local π – π^* transitions³⁵. Absorption peaks emerged at ca. 730 nm for (s,s,s,s)-DPP6T, (R,R,R,R)-DPP6T where the peak at ca. 740 nm for (s,s)-DPP6T and (R,R)-DPP6T films (solid lines in Fig. 1c and Supplementary Fig. 2), which were attributed to the intermolecular π – π stacking in solid films. Meanwhile, the hypochromatical shifted ICT peaks indicate the favored H-aggregation between donor molecules in these films³³.

These chiral DPP6T donors were CD silent in solutions in near UV–vis (NUV–vis) regions (Supplementary Fig. 3). However, supramolecular chirality was easily built in the DPP6T films via intermolecular π – π stacking, which resulted in the sufficient and expanded CD absorption bands of the films in almost all of the NUV–vis regions (Fig. 1d and Supplementary Fig. 4). In (s,s,s,s)- and (R,R,R,R)-DPP6T films, the bisignate CD bands at ca. 390 and 430 nm corresponded to the absorption peak at ca. 420 nm in the UV–vis spectrum, which stemmed from the distinct exciton coupling of the intramolecular π – π^* transitions. The bisignate CD bands that appeared at 540 and 650 nm corresponded to the main absorption peak at ca. 600 nm in the UV–vis spectrum, which was derived from intramolecular chiral charge transfer. The CD bands that appeared at ca. 740 nm corresponded to the absorption peak at ca. 740 nm in the UV–vis spectrum, which was derived from the intermolecular chiral π – π transitions. The CD absorption was much weaker in the (s,s)- and (R,R)-DPP6T films than in the (s,s,s,s)- and (R,R,R,R)-DPP6T films as determined by measuring films with comparative thickness (Fig. 1d and corresponding *g*-factor see Supplementary Fig. 4). The films from DPP6T attaching s and R pendants showed mirrored CD spectra but identical UV–vis spectra. This result revealed that the enantiomeric stereocenters of the peripheral alkyl chains induced the supramolecular chirality in the DPP6T aggregations.

In comparison with the neat DPP6T films, the DPP6T donors added with PC₆₁BM acceptors showed no defined effect on the light absorption of the DPP6T counterpart (Fig. 1e). However, the CD intensity remarkably reduced in the (s,s)- and (R,R)-DPP6T based blends comparing with their neat films, but no

distinct CD decline was observed in the (s,s,s,s)- and (R,R,R,R)-DPP6T based blends (Fig. 1d and f, an enlarged view is presented in Supplementary Fig. 5). In addition, no specific induced chirality belonging to the PC₆₁BM acceptor was observed in the blends (Fig. 1f), indicating that no distinctive interaction existed between the DPP6T donors and PC₆₁BM acceptors at a supramolecular level. The changes in the CD and UV-vis spectra indicated that explicit phase separation might occur between the donor and the acceptor in the blends. Furthermore, increasing the amount of enantiomeric side chains intensified such phase separation and resulted in CD intensity maintenance in the (s,s,s,s)- and (R,R,R,R)-DPP6T counterparts in the blends.

Interestingly, no distinct helical chirality was observed in neither neat nor blended DPP6T films, though right-handed (s,s,s,s)-DPP6T nanofibers and left-handed (R,R,R,R)-DPP6T nanofibers were observed from their precipitations via a fast self-assembly process in solution (Fig. 1g and h, detail see Supplementary Method 2). The molecular chirality from these enantiopure DPP6T transferred to the nanoscale helical chirality of the assemblies via helical intermolecular π - π stacking and these helical nanofibers possess accordant CD and UV features with their film counterparts (Supplementary Fig. 6). As CD originates from the electronic transitions of the chromophore and provides detailed information on chiral interaction^{26,27}. These results indicated that though the expression of such nanoscale helical chirality was restricted in spin-coating films, they share consistence intermolecular distance and twisting orientation with their helical fibril counterparts thus their chiroptically generated excitons were retained. The similar phenomenon was observed in a blended film of achiral polyfluorene polymer with a chiral helicene derivative by Yang et al³⁶. The blended films exhibited strong chiroptical properties despite that no helical structure was observed in the isotropic granular nanoscale morphology. This result would be further verified through the structural and morphological analysis of the neat and blended films.

Molecular stacking and morphological characteristics of the neat and blended chiral films. Grazing incidence wide-angle X-ray scattering (GIWAXS) measurements were conducted to characterize the molecular stacking and crystallinity of the neat films and blended active layers. The neat (R,R,R,R)- and (s,s,s,s)-DPP6T films presented lamellar peaks in both in-plane (IP) and out-of-plane (OOP) directions at $q = 0.21 \text{ \AA}^{-1}$ (Fig. 2a and b; corresponding integration in Supplementary Fig. 7a and b). The multiple high-order diffraction peaks in the OOP direction at $q = 0.21, 0.44, 0.66, 0.86 \text{ \AA}^{-1}$ could be assigned to (100), (200), (300) and (400) reflections, respectively, which were attributed to the ordered arrangement along the chiral alkyl-stacking direction. The neat (R,R)- and (s,s)-DPP6T films showed distinct diffraction peaks at $q = 0.56 \text{ \AA}^{-1}$ ($d = 11.22 \text{ \AA}$) and $q = 1.14 \text{ \AA}^{-1}$ ($d = 5.51 \text{ \AA}$) in the OOP direction corresponding to (200) and (400) reflections, respectively (Fig. 2c and d; corresponding integration in Supplementary Fig. 7c and d). The distinct scattering points indicated a remarkable crystallinity in the neat (R,R)- and (s,s)-DPP6T films with smaller d -spacing in the (100) direction than that in the neat (R,R,R,R)- and (s,s,s,s)-DPP6T films because of less amounts of chiral side chains. The evident (010) reflection of π - π stacking in the IP direction at $q = 1.82 \text{ \AA}^{-1}$ ($d = 3.45 \text{ \AA}$) indicated the preferred edge-on molecular packing orientation with respect to the substrate in the (R,R)- and (s,s)-DPP6T films. However, no such molecular orientation was observed in the (R,R,R,R)- and (s,s,s,s)-DPP6T films.

Upon PC₆₁BM addition, the changes that appeared in the diffraction peaks in the (R,R)- and (s,s)-DPP6T counterparts of the corresponding blends (Fig. 2g and h; corresponding integration in Supplementary Fig. 7c and d) were more pronounced than those in the (R,R,R,R)- and (s,s,s,s)-DPP6T:PC₆₁BM blends (Fig. 2e and f; corresponding integration in Supplementary Fig. 7a and b). The sharp diffraction peaks in the neat (R,R)- and (s,s)-DPP6T fused into diffraction rings while being blended with PC₆₁BM. Conversely, the diffraction patterns of the donor counterpart in the (R,R,R,R)- and (s,s,s,s)-DPP6T:PC₆₁BM blends were almost the same as those of the neat films. The PC₆₁BM likely led to the more pronounced effect on preventing the overaggregation of the (R,R)- and (s,s)-DPP6T in the blends than that in the (R,R,R,R)- and (s,s,s,s)-DPP6T:PC₆₁BM systems. Increasing enantiomeric alkyl side chains contributes to maintaining the CD intensity of the (R,R,R,R)- and (s,s,s,s)-DPP6T:PC₆₁BM blends by producing preferred donor aggregations.

The morphology of the films was characterized via atomic force microscopy (AFM) and transmission electron microscopy (TEM). In the AFM height images (Fig. 2i, j, k and l), large roundish domains formed in the (R,R,R,R)- and (s,s,s,s)-DPP6T:PC₆₁BM films, whereas small fibril domains formed in the (R,R)- and (s,s)-DPP6T:PC₆₁BM films. The (R,R,R,R)-DPP6T:PC₆₁BM and (s,s,s,s)-DPP6T:PC₆₁BM films demonstrated their root-mean-square surface roughness (R_q) of 5.90 and 5.44 nm, respectively, which were evidently higher than those of the (R,R)-DPP6T:PC₆₁BM (1.38 nm) and (s,s)-DPP6T:PC₆₁BM films (1.29 nm). The TEM images confirmed the aggregation states of the blends in the bulk (Fig. 2m, n, o and p). The molecular interactions between conjugated donors and acceptors governed the morphological formation and purity of the mixed domains in the blends and consequently controlled the achievable performance of OSCs.

Photovoltaic performance of chiral DPP6T:PC₆₁BM-based OSC devices Conventional devices with an architecture of ITO/poly(3,4-ethylenedioxythiophene):poly(styrenesulfonate) (PEDOT:PSS)/DPP6T:PC₆₁BM/Al were constructed (Fig. 1a). The current density–voltage ($J-V$) characteristics were measured under AM 1.5 G illuminations with an intensity of 100 mW cm⁻² (Supplementary Fig. 8). The comprehensive photovoltaic performance is summarized in Supplementary Table 1. The chiral OSCs based on enantiomeric DPP6T donors exhibited a comparable photovoltaic performance, whereas the photovoltaic performance decreased as the amount of peripheral alkyl chains increased. The comprehensive optimization of device performance were presented in Supplementary Tables 2 and 3. In detail, the (s,s)- and (R,R)-DPP6T:PC₆₁BM-based devices yielded a power conversion efficiency (PCE) of around 1.96% with an open-circuit voltage (V_{oc}) of 0.65 V, a short-circuit current density (J_{sc}) of 8.08 mA cm⁻² and a fill factor (FF) of 37.29%. With the amount of peripheral alkyl chains achieved to four, the PCE of the (s,s,s,s)- and (R,R,R,R)-DPP6T:PC₆₁BM-based devices decreased to around 1.31% with a V_{oc} of 0.63 V, a J_{sc} of 3.73 mA cm⁻² and a FF of 55.77%. These differences in photovoltaic performance should be attributed to the difference in molecular stacking and, in turn, the morphological characteristics of the discussed chiral DPP6T:PC₆₁BM active layers.

Direct detection of CPL by chiral OSCs

The chiral OSCs were used to conduct CPL detection under ambient conditions. The excitation wavelengths were selected on the basis of the CD maximums (valleys and peaks) and minimums (crossovers) of the chiral blends. The $I-T$ switching characteristics were explored by turning the l- or r-CPL on and off with a cycle period of 40 s (Fig. 3a, b, c and d; Supplementary Figs. 9, 10, 11 and 12). The self-powered photovoltaic short-circuit current (I_{sc}) was coupled with the handedness of CPL. For example, in the chiral OSCs based on (s,s,s,s)-DPP6T, the CPL irradiation at CD maximums (around 426, 540, 606, and 640 nm) with either correct or opposite handedness caused an increase in I_{sc} of chiral OSCs, but the CPL irradiation with the correct handedness caused a more pronounced increase (Fig. 3a and Supplementary Fig. 9a, c and f). This was owing to the fact that CPL irradiations with the correct handedness induced a more efficient photon absorption than the opposite ones, resulting in a relatively higher density of exciton generation in the chiral active layers. The photo-induced excitons subsequently dissociated into free charge carriers in the BHJ active layers and the predominant carrier density induced by the correct CPL brought about a more pronounced increase in I_{sc} than that by the opposite CPL. Whereas, the CPL irradiation at CD minimums (around 475 and 570 nm) with both the correct and opposite handedness caused a strong but indiscriminate increase in I_{sc} because the CD minimums coincided with the absorption maximums with an efficient light absorption (Supplementary Fig. 9b and d). The detection scenario was similar but was mirrored by using the (r,r,r,r)-DPP6T-based chiral OSC because of the mirrored chiroptical properties (Fig. 3b and Supplementary Fig. 10a–f). The OSCs based on the (s,s)- and (r,r)-DPP6T presented obscure detection sensitivity on CPL owing to their weak chiroptical absorption (Fig. 3c and d; Supplementary Figs. 11 and 12).

To further quantitatively assess the relationship between the CPL detection performance and g -factor of OSCs, we introduced the device metrics, including the dissymmetry factor of short-circuit current (g_{sc}), responsivity (R), and specific detectivity (D^*) to quantify the relative difference in I_{sc} , the strength of the photoresponse, as well as the noise equivalent power to the device area and electrical bandwidth of the noise measurement upon alternating irradiation of l- and r-CPL^{19,21}. We introduced the g -factor as it is in favor of the lateral comparison of CD intensity among the samples²⁷. The g -factor of the (s,s,s,s)- and (r,r,r,r)-DPP6T:PC₆₁BM-based OSCs were in the 10^{-2} order of magnitude, which was two orders of magnitude higher than that in the 10^{-4} order of magnitude from (s,s)- and (r,r)-DPP6T:PC₆₁BM-based OSCs (Fig. 3e and i). The g_{sc} , R , and D^* were calculated using the following equations:

$$g_{sc} = 2 \frac{I_l - I_r}{I_l + I_r} \quad (1)$$

$$R = \frac{J_{ph}}{L_{light}} \quad (2)$$

$$D^* = \frac{J_{ph}/L_{light}}{(2qJ_d)^{1/2}} \quad (3)$$

where J_{ph} is the photocurrent, L_{light} is the incident intensity, J_d is the dark current and q is the elementary charge. The g_{sc} of the (s,s)- and (R,R)-DPP6T:PC₆₁BM-based OSCs were almost one order of magnitude lower than that of the (s,s,s,s)- and (R,R,R,R)-DPP6T:PC₆₁BM-based OSCs. For example, the (s,s,s,s)- and (R,R,R,R)-DPP6T:PC₆₁BM-based OSCs demonstrated their maximum g_{sc} of -0.127 ± 0.003 and 0.171 ± 0.004 at 606 nm, respectively. However, the (s,s)- and (R,R)-DPP6T:PC₆₁BM-based OSCs demonstrated their maximum g_{sc} of only -0.0113 and 0.0143 , respectively (Fig. 3f and j). The error bar in the figures was obtained from 10 repeated measurements. The signs of g_{sc} by using alternating OSCs with enantiomeric chirality were opposite. With the g -factor of the OSCs enhanced in the order of magnitudes from 10^{-4} to 10^{-2} , their g_{sc} was clearly increased in the order of magnitudes from 10^{-2} to 10^{-1} .

We also calculated R and D^* at the selected wavelengths of CD maximums and minimums. The maximum values of R were estimated to be 0.36, 0.11, 0.21 and 0.29 $A W^{-1}$ for the (s,s,s,s)-, (R,R,R,R)-, (s,s)-, and (R,R)-DPP6T:PC₆₁BM-based OSCs, respectively, which were two order of magnitude larger than those based on chiral plasmonic metamaterials ($0.0022 A W^{-1}$)¹³ also comparable with the best reported 1D perovskite CPL detectors ($0.797 A W^{-1}$)¹⁴ and the commercialized Si photodiode ($1 A W^{-1}$)³⁷. The maximum values of D^* were 1.94×10^{13} , 5.61×10^{12} , 1.03×10^{13} and 2.17×10^{13} Jones (Jones = $cm Hz^{1/2} W^{-1}$) for the (s,s,s,s)-, (R,R,R,R)-, (s,s)-, and (R,R)-DPP6T:PC₆₁BM-based OSCs, respectively (Supplementary Fig. 13). These values were one order of magnitude higher than those of the best reported quasi-2D perovskite CPL detectors (1.1×10^{12} Jones)¹⁵ recently as well as those of the commercialized Si photodiode (10^{12} Jones)³⁷. The detailed comparisons are presented in Supplementary Table 4. Additionally, while the g -factor of the OSCs was enhanced in the order of magnitudes, the ΔR and ΔD^* (the relative differences in R and D^* upon the alternating irradiation of l- and r-CPL, respectively) amplified in the order of magnitudes (Fig. 3g, h, k, and i). The results suggested that the response to the CPL of chiral OSCs was consistent with the CD spectrum in the position and intensity of CD absorption bands. The enhanced g -factor enabled the enhanced distinguishability of chiral OSCs between l- and r-CPL; for example, the better selectivity was obtained in the (s,s,s,s)- and (R,R,R,R)-DPP6T:PC₆₁BM-based OSCs than that in the (s,s)- and (R,R)-DPP6T:PC₆₁BM-based OSCs. The highest ΔR (ca. $40 mA W^{-1}$) was obtained in the (s,s,s,s)-DPP6T-based OSCs at 606 nm, which was four times higher than that of the best reported 1D perovskite CPL detectors (ca. $10 mA W^{-1}$, Supplementary Table 4)¹⁴.

We extensively explored how the intensity of the incident CPL and the thickness of chiral active layers influence the CPL detection sensitivity of OSCs because of their great importance in practical CPL detection. The intensity of photocurrent under CPL irradiation was positively dependent on the incident light intensity at given wavelengths, such as 540, 606 and 640 nm, by using (R,R,R,R)-DPP6T:PC₆₁BM OSCs (Fig. 4a, and b; Supplementary Fig. 14a); the enhanced irradiation intensity generates increased densities of photon-excited electron–hole pairs and consequently leads to enhanced J_{sc} ³⁸. Significantly, both the J_{sc} and the relative difference in J_{sc} upon alternating irradiation of l- and r-CPL exhibited positively linear increase as the CPL intensity increased (in a double logarithm scale) (Fig. 4c, d, and Supplementary Fig. 14b). The broad detection in the intensity range of CPL is highly important in practical CPL detection³², though we could not measure the linear dynamic range (LDR) of these chiral OSCs at the present stage because of the intensity limitation of our CPL source. R and D^* were negatively correlated with the intensity of CPL, indicating the detection potential of the chiral OSCs upon weak CPL irradiation. Using the formula derivation, we deduced that the g_{sc} , g_R , and g_{D^*} , which are the dissymmetry factors of J_{sc} , R , and D^* , respectively, were independent of the CPL intensity (Fig. 4c–f; Supplementary Fig. 14b and 15a, b; Supplementary Note 1). These three parameters are crucial in the real-world applications, which can be used to accurately perform CPL detection without considering the CPL intensity.

To interpret how the thickness of the chiral active layer influences chiroptical responses, we fabricated OSCs with a series of active layer thicknesses. For example, in (R,R,R,R)-DPP6T:PC₆₁BM-based OSCs with chiral active layer thicknesses of 53, 72, 80, 89 and 124 nm, as the thickness increased, the g -factor unexpectedly increased until the thickness reached ca. 100 nm (Fig. 4g, and h). The g -factor should be independent of sample concentration and optical pathlength in a proper range²⁷; however, a thickness of <100 nm was too thin to fit in such a range, which led to a decrease in the g -factor. The g_{sc} also decreased because of the decrease in g -factor of the chiral active layer (Fig. 4i; Supplementary Fig. 16). This result further revealed that the g -factor of the active layers played a key role in the CPL detection sensitivity of chiral OSCs. However, the saturation of g_{sc} lagged behind that of the g -factor as the thickness of the chiral active layers increased (Fig. 4i). Very thin active layers (e.g., <100 nm) were deficient in light absorption and could result in CPL reflection from metal electrodes in OSCs. The reflected light would present a reversed handedness from the incident CPL¹¹. As a consequence, the absorption of the reflected CPL with the reversed handedness by the active layer leading to such lag in g_{sc} . Chiral OSCs with active layers thicker than 130 nm may suffer from charge recombination due to long exciton diffusion length; as such, 100–130 nm should be the optimal thickness for effective CPL detection applied to the present case. This finding further revealed that the thickness of chiral active layers is highly important in chiral optoelectronic devices³⁹⁻⁴¹.

Discussion

In summary, we built supramolecular chirality in OSCs by using enantiomeric DPP6T donors and achiral PC₆₁BM acceptors. The supramolecular chirality of the OSCs was explicitly coupled to the polarization

state of CPL with a positive CD absorption responding to l-CPL and a negative CD absorption to r-CPL. The detection scenario was analogous to Cotton effect from the supramolecular chirality of donor aggregations, though their molecular chirality in relevant wavelengths was silent. As the g -factor in the active layers increased, the crucial device metrics for CPL direct detection, including g_{sc} , relative differences in responsivity (ΔR) and specific detectivity (ΔD^*) upon the alternating irradiation of l- and r-CPL, were drastically enhanced. By further exploring the performance of these chiral OSCs by adjusting both intrinsic and external parameters, mainly the thickness of chiral active layers and the intensity of incident CPL, we found that g_{sc} , g_R , and g_{D^*} were independent of CPL intensity, revealing their great feasibility in the practical CPL direct detection under ambient conditions. Given that the enhanced g -factor and expanded CD absorption in organic semiconductors via the principle of supramolecular chirality are unique with vast spaces and ample approaches for further technical evolution, the strategy we demonstrated here is likely to act as one of the most potent ones to constantly promote the development of direct CPL detection.

Methods

Synthesis of chiral DPP6T molecules. (s)- and (R)-1-Bromo-3,7-dimethyloctane were used as alkylating agents to attach to the lactam nitrogen atom of diketopyrrolopyrrole–thiophene double-bromide molecule with potassium carbonate as the base. The reaction occurred in dimethylformamide at 120 °C. The organotin compound of bithiophene or chiral alkylated bithiophene was selected to react with the molecules we attained in the previous step via Pd-[PPh₃]₄-catalyzed Stille coupling reaction. The structure and molecular weight of chiral DPP6T molecules were confirmed through nuclear magnetic resonance (AVANCE III HD 400) and matrix-assisted laser desorption ionization–time-of-flight mass spectrometry, respectively. The similar synthetic procedures of these small molecules could be found in the previous work⁴². The detailed synthetic procedures were presented in the Supplementary Method 1 and Supplementary Fig. 17–22.

UV–vis absorption, CD, and molecular energy-level measurements. UV–vis absorption and CD spectra were obtained on a UV-3600 (Shimadzu) spectrophotometer and J-1500 (Jasco), respectively. Energy levels were conducted via CV measurement on an electrochemical station (VMP3 Biologic, France), where 0.1 mol L⁻⁴ tetrabutylammonium phosphorus hexafluoride acetonitrile solution served as an electrolyte with a scan rate of 50 mV s⁻¹. The Pt electrode coated with a chiral DPP6T molecule, a Pt plate and an Ag/Ag⁺ electrode was used as working, counter and reference electrodes, respectively. Redox potentials were internally calibrated using a ferrocene/ferrocenium (Fc/Fc⁺) redox couple (- 4.8 eV).

Device preparation and performance measurement. Conventional devices were fabricated with a structure of glass/ITO/PEDOT:PSS/DPP6T:PC₆₁BM/Al. The ITO-coated glass substrates were sequentially cleaned with detergent, deionized water, ethyl alcohol and isopropyl alcohol under 20 min of ultrasonication for each step. A PEDOT:PSS layer was spin-coated at 3,000 rpm min⁻¹ onto the ITO substrate. After being baked at 150 °C for 15 min, the substrates were transferred into a nitrogen-filled glove box. The

DPP6T:PC₆₁BM (1:1) blends were fully dissolved in CF at a total weight concentration of ca. 17 mg mL⁻¹. Subsequently, the mixture solution was spin-coated at a rate of 1500 rpm min⁻¹ to form the active layer. The blend films were thermally annealed at 100 °C for 10 min. An 80 nm-thick Al layer was evaporated onto the active layer under high vacuum (ca. 1 × 10⁻⁵ Pa). Device *J–V* characteristics were measured under AM 1.5 G (100 mW cm⁻²) illuminations by using a Newport Thermal Oriel 91159A solar simulator. Light intensity was calibrated with a Newport Oriel PN 91150V Si-based solar cell. *J–V* characteristics were recorded using a Keithley 2400 source-measure unit. Device areas of each cell was approximately 4 mm².

AFM, TEM, and GIWAXS characterizations. AFM height images were recorded on a Multimode-8 Nanoscope (Bruker). The spin-coated films for the AFM measurements were fabricated in the same condition for OSCs. TEM characterization was conducted on Tecnai G2 F20 U-TWIN (FEI Co., USA) under an operating voltage of 200 KV. Films for the TEM test were made by spin-coating in the same condition for solar cell devices on ITO substrates. After 100 °C thermal annealing for 10 min, the blended films were immersed in water and the floating active layers were transferred to the carbon-coated copper grid. GIWAXS measurements were conducted on a XEUSS SAXS/WAXS system (XENOCSS, France). The blended and neat films for GIWAXS measurements were made by the same method for OSCs active layer on Si/PEDOT:PSS substrates.

Direct CPL detection. CPL detection was performed using the same architecture as that for OSCs. CPL illumination was obtained using a linear polarizer and a quarter-wave plate. The achromatic quarter-wave plate with flat retardance over broad wavelength ranges bought from Thorlabs (American). The specification of the quarter-wave plate we used is AQWP05M-340 (260–410 nm, Average Reflectance < 0.5%, wave plate material is Crystalline Quartz & UV Sapphire), AQWP05M-600 (400–800 nm, Average Reflectance < 0.5%, wave plate material is Crystalline Quartz & Magnesium Fluoride). *I–T* curves were measured using Keithley 4200-SCS in an electromagnetically shielded probe station. Combined the CD and UV–vis spectrum, photoexcitation was carried out using the monochromatic light with wavelengths of 426 nm (22.3 μW cm⁻²), 475 nm (19.5 μW cm⁻²), 540 nm (15.7 μW cm⁻²), 570 nm (13.1 μW cm⁻²), 606 nm (10.3 μW cm⁻²) and 640 nm (8.52 μW cm⁻²) for the (s,s,s)- and (s,s,s,s)-DPP6T, whereas, 390 nm (25.8 μW cm⁻²), 490 nm (19.5 μW cm⁻²), 576 nm (13.0 μW cm⁻²) and 641 nm (8.5 μW cm⁻²) for the (s,s)- and (s,s,s)-DPP6T, corresponding to the valleys, peaks and crossovers in the CD spectra. The CPL intensity was recorded by an optical power meter (S120VC) with a measurable power range of 50 nW–50 mW and a measurable wavelength range of 200–1100 nm, which was bought from Thorlabs (American).

Declarations

Competing Interests:

The authors declare no competing interests.

Author Contributions

Z.W. planned the project and supervised the research. L.L. and Y.Y. designed and conducted the experiments, carried out data analysis, and developed the working mechanism. L.L. and Y.Y. prepared the OSC devices and performed the characterizations, with contributions from Y.Z.. Y.Y. and L.L. synthesized the molecules. J.Z. conducted X-ray scattering characterization. L.L., Y.Y. and W.Z. wrote the manuscript. W.A.M. contributed in language corrections. L.L. and Y.Y. contributed equally to this work.

Acknowledgements

The authors acknowledge the financial support from the Ministry of Science and Technology of China (Grant no. 2016YFA0200700), the National Natural Science Foundation of China (Grant nos. 21534003 and 21721002), the China Postdoctoral Science Foundation (Grant no. 2019M660584), and the Chinese Academy of Sciences.

References

1. Templin, R. M., How, M. J., Roberts, N. W., Chiou, T.-H. & Marshall, J. Circularly polarized light detection in stomatopod crustaceans: a comparison of photoreceptors and possible function in six species. *J. Exp. Biol.* **220**, 3222–3230 (2017).
2. Bok, M. J., Porter, M. L., Place, A. R. & Cronin, T. W. Biological Sunscreens Tune Polychromatic Ultraviolet Vision in Mantis Shrimp. *Curr. Biol.* **24**, 1636–1642 (2014).
3. Cronin, T. W., Chiou, T.-H., Caldwell, R. L., Roberts, N. & Marshall, J. in *Polarization Science and Remote Sensing Iv* Vol. 7461 *Proceedings of SPIE* (eds J. A. Shaw & J. S. Tyo) (2009).
4. Gagnon, Y. L., Templin, R. M., How, M. J. & Marshall, N. J. Circularly Polarized Light as a Communication Signal in Mantis Shrimps. *Curr. Biol.* **25**, 3074–3078 (2015).
5. Brooks, W. H., Guida, W. C. & Daniel, K. G. The Significance of Chirality in Drug Design and Development. *Curr. Top. Med. Chem.* **11**, 760–770 (2011).
6. Sherson, J. F. *et al.* Quantum teleportation between light and matter. *Nature* **443**, 557–560 (2006).
7. Farshchi, R., Ramsteiner, M., Herfort, J., Tahraoui, A. & Grahm, H. T. Optical communication of spin information between light emitting diodes. *Appl. Phys. Lett.* **98**, 162508 (2011).
8. Schadt, M. Liquid crystal materials and liquid crystal displays. *Annual Review of Materials Science* **27**, 305–379 (1997).
9. Chiou, T.-H. *et al.* Circular polarization vision in a stomatopod crustacean. *Curr. Biol.* **18**, 429–434 (2008).

10. Kim, D.-Y. Potential application of spintronic light-emitting diode to binocular vision for three-dimensional display technology. *J. Korean Phys. Soc.* **49**, S505-S508 (2006).
11. Yang, Y., da Costa, R. C., Fuchter, M. J. & Campbell, A. J. Circularly polarized light detection by a chiral organic semiconductor transistor. *Nat. Photonics* **7**, 634–638 (2013).
12. Shang, X. *et al.* Supramolecular Nanostructures of Chiral Perylene Diimides with Amplified Chirality for High-Performance Chiroptical Sensing. *Adv. Mater.* **29**, 1605828 (2017).
13. Li, W. *et al.* Circularly polarized light detection with hot electrons in chiral plasmonic metamaterials. *Nat. Comm.* **6**, 8379 (2015).
14. Chen, C. *et al.* Circularly polarized light detection using chiral hybrid perovskite. *Nat. Comm.* **10**, 1927 (2019).
15. Wang, L. *et al.* Chiral Reduced-Dimension Perovskite for an Efficient Flexible Circularly Polarized Light Photodetector. *Angew. Chem. Int. Ed.*, **59**, 6442–6450 (2020).
16. Gilot, J. *et al.* Polymer Photovoltaic Cells Sensitive to the Circular Polarization of Light. *Adv. Mater.* **22**, E131-E134, (2010).
17. Schulz, M. *et al.* Chiral Excitonic Organic Photodiodes for Direct Detection of Circular Polarized Light. *Adv. Func. Mater.* **29**, 1900684 (2019).
18. Long, G. *et al.* Chiral-perovskite optoelectronics. *Nat. Rev. Mater.*, **5**, 423–439 (2020).
19. García de Arquer, F. P., Armin, A., Meredith, P. & Sargent, E. H. Solution-processed semiconductors for next-generation photodetectors. *Nat. Rev. Mater.* **2**, 16100 (2017).
20. Orji, N. G. *et al.* Metrology for the next generation of semiconductor devices. *Nature electronics* **1**, 532–547 (2018).
21. Schulz, M. *et al.* Chiral Excitonic Organic Photodiodes for Direct Detection of Circular Polarized Light. *Adv. Funct. Mater.* **29**, 1900684 (2019).
22. Li, W. *et al.* Circularly polarized light detection with hot electrons in chiral plasmonic metamaterials. *Nat. Commun.* **6**, 8379 (2015).
23. Chu, Z. *et al.* Circular Polarization Discrimination Enhanced by Anisotropic Media. *Adv. Opt. Mater.*, **8**, 1901800 (2020).
24. Yang, Y., Zhang, Y. & Wei, Z. Supramolecular Helices: Chirality Transfer from Conjugated Molecules to Structures. *Adv. Mater.* **25**, 6039–6049 (2013).
25. Hoeben, F. J. M., Jonkheijm, P., Meijer, E. W. & Schenning, A. About supramolecular assemblies of pi-conjugated systems. *Chem. Rev.* **105**, 1491–1546 (2005).
26. Pescitelli, G., Bari, L. & Berova, N. Application of electronic circular dichroism in the study of supramolecular systems. *Chem. Soc. Rev.* **43**, 5211–5233, doi:10.1039/c4cs00104d (2014).
27. Berova, N., Di Bari, L. & Pescitelli, G. Application of electronic circular dichroism in configurational and conformational analysis of organic compounds. *Chem. Soc. Rev.* **36**, 914–931 (2007).
28. Heeger, A. J. 25th Anniversary Article: Bulk Heterojunction Solar Cells: Understanding the Mechanism of Operation. *Adv. Mater.* **26**, 10–28 (2014).

29. Pierre, A., Deckman, I., Lechene, P. B. & Arias, A. C. High Detectivity All-Printed Organic Photodiodes. *Adv. Mater.* **27**, 6411–6417 (2015).
30. Gong, X. *et al.* High-Detectivity Polymer Photodetectors with Spectral Response from 300 nm to 1450 nm. *Science* **325**, 1665–1667 (2009).
31. Zhang, L. Z. *et al.* Toward Highly Sensitive Polymer Photodetectors by Molecular Engineering. *Adv. Mater.* **27**, 6496–6503 (2015).
32. de Arquer, F. P. G., Armin, A., Meredith, P. & Sargent, E. H. Solution-processed semiconductors for next-generation photodetectors. *Nat. Rev. Mater.* **2**, 16100 (2017).
33. Kirkus, M. *et al.* Optical Properties of Oligothiophene Substituted Diketopyrrolopyrrole Derivatives in the Solid Phase: Joint J- and H-Type Aggregation. *J. Phys. Chem. A* **116**, 7927–7936 (2012).
34. Nielsen, C. B., Turbiez, M. & McCulloch, I. Recent Advances in the Development of Semiconducting DPP-Containing Polymers for Transistor Applications. *Adv. Mater.* **25**, 1859–1880 (2013).
35. Kirkus, M. *et al.* Optical Properties of Oligothiophene Substituted Diketopyrrolopyrrole Derivatives in the Solid Phase: Joint J- and H-Type Aggregation. *J. Phys. Chem. A* **116**, 7927–7936 (2012).
36. Yang, Y., da Costa, R. C., Smilgies, D.-M., Campbell, A. J. & Fuchter, M. J. Induction of Circularly Polarized Electroluminescence from an Achiral Light-Emitting Polymer via a Chiral Small-Molecule Dopant. *Adv. Mater.* **25**, 2624–2628 (2013).
37. Carey, J. E., Crouch, C. H., Shen, M. Y. & Mazur, E. Visible and near-infrared responsivity of femtosecond-laser microstructured silicon photodiodes. *Opt. Lett.* **30**, 1773–1775 (2005).
38. Clarke, T. M. & Durrant, J. R. Charge Photogeneration in Organic Solar Cells. *Chemical Reviews* **110**, 6736–6767 (2010).
39. Yang, Y. *et al.* Emergent Properties of an Organic Semiconductor Driven by its Molecular Chirality. *ACS Nano* **11**, 8329–8338 (2017).
40. Brandt, J. R., Wang, X., Yang, Y., Campbell, A. J. & Fuchter, M. J. Circularly Polarized Phosphorescent Electroluminescence with a High Dissymmetry Factor from PHOLEDs Based on a Platinahelicene. *J. Am. Chem. Soc.* **138**, 9743–9746 (2016).
41. Wan, L. *et al.* Inverting the Handedness of Circularly Polarized Luminescence from Light-Emitting Polymers Using Film Thickness. *ACS Nano* **13**, 8099–8105 (2019).
42. Back, J. Y. *et al.* Investigation of Structure-Property Relationships in Diketopyrrolopyrrole-Based Polymer Semiconductors via Side-Chain Engineering. *Chem. Mater.* **27**, 1732–1739 (2015).

Figures

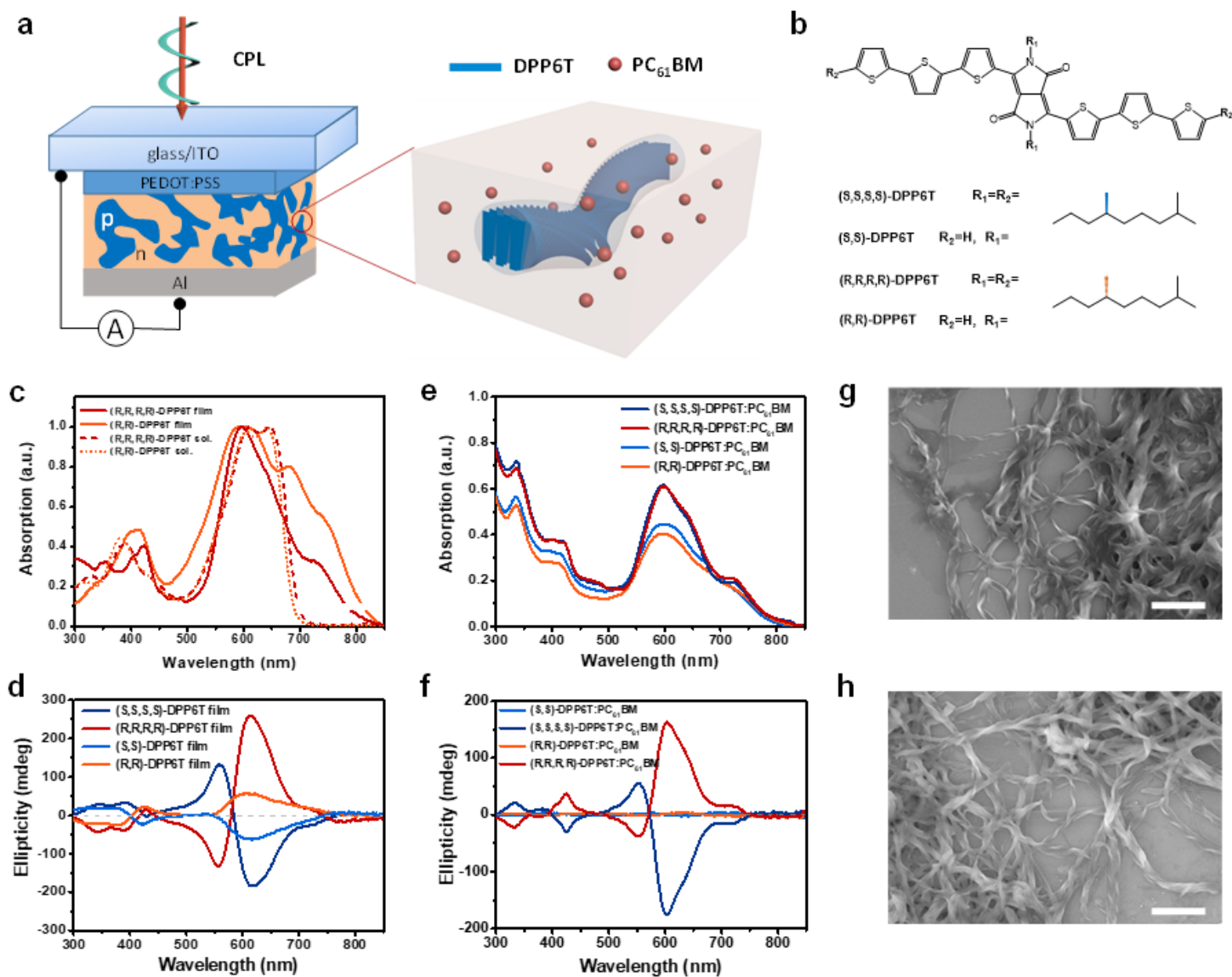


Figure 1

Experimental setup, molecular structure, and optical and electrochemical properties. **a** The scheme demonstrates the experimental setup of chiral OSCs for CPL detection, in which the DPP6T donor with helical intermolecular aggregation was blended with achiral PC₆₁BM acceptors as active layer. **b** Molecular structure of chiral DPP6T donors. **c** UV-vis spectra of the solutions and neat films of (R,R,R,R)- and (R,R)-DPP6T. **d** CD spectra of the neat films of chiral DPP6T donors. **e** and **f** UV-vis and CD spectra of chiral (s,s)-, (s,s,s,s)-, (R,R,R,R)- and (R,R)-DPP6T donors blended with PC₆₁BM acceptors. **g** and **h** SEM images of (s,s,s,s)- and (R,R,R,R)-DPP6T assemblies via fast self-assembly in solution. The scale bars of SEM images in **g** and **h** correspond 1 μm.

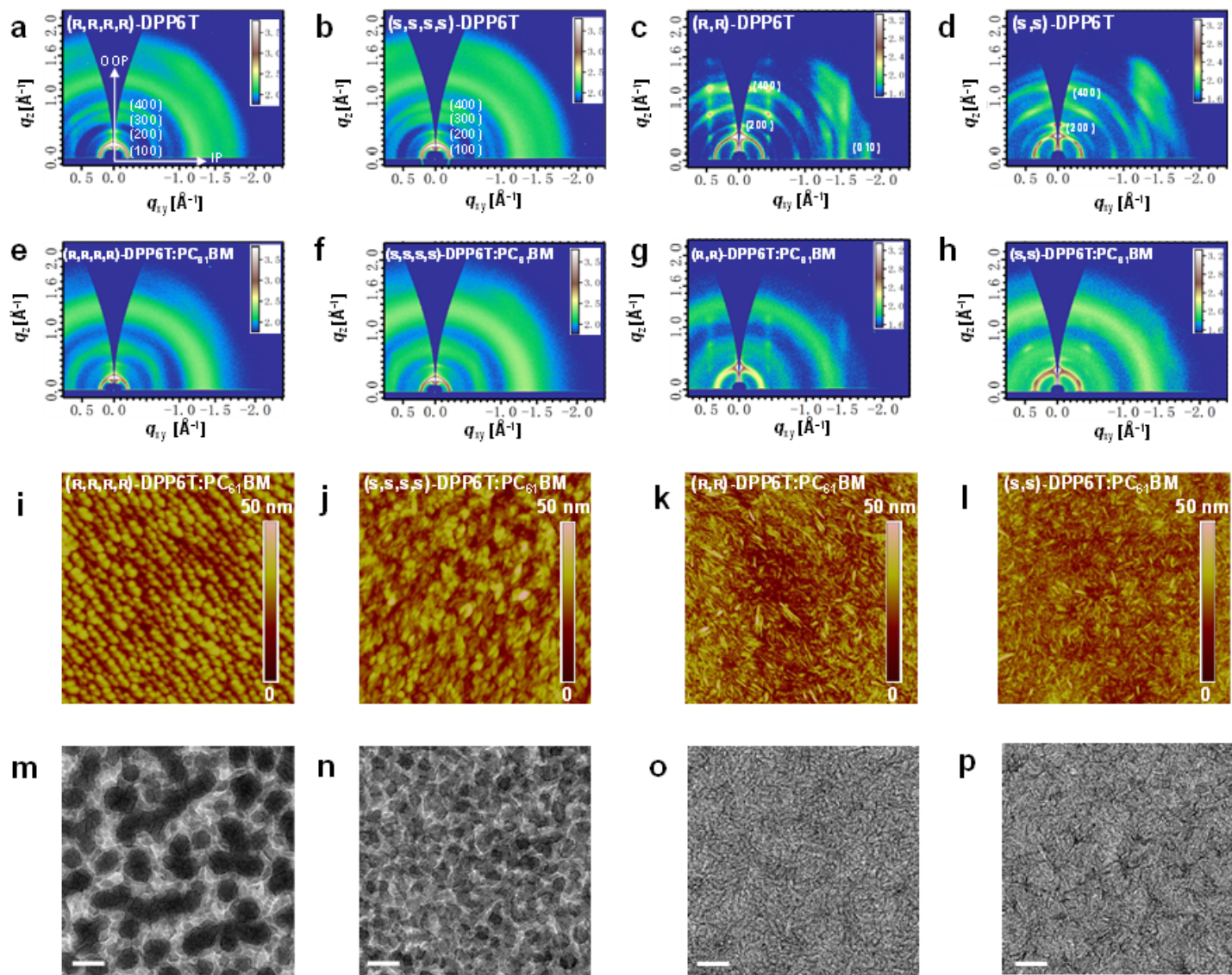


Figure 2

Molecular stacking and morphology of the neat and blended chiral films. a, b, c and d. 2D-GIWAXS patterns of the corresponding neat films of the chiral donors (R,R,R,R)-, (S,S,S,S)-, (R,R)- and (S,S)-DPP6T. e, f, g and h 2D-GIWAXS patterns of the corresponding blended films of (R,R,R,R)-, (S,S,S,S)-, (R,R)- and (S,S)-DPP6T:PC61BM. i, j, k and l AFM height images (5 $\mu\text{m} \times 5 \mu\text{m}$) of the corresponding blended films of (R,R,R,R)-, (S,S,S,S)-, (R,R)- and (S,S)-DPP6T:PC61BM. m, n, o and p TEM images of the corresponding blended films of (R,R,R,R)-, (S,S,S,S)-, (R,R)- and (S,S)-DPP6T:PC61BM. Scale bars of TEM images in m, n, p and q correspond 0.2 μm .

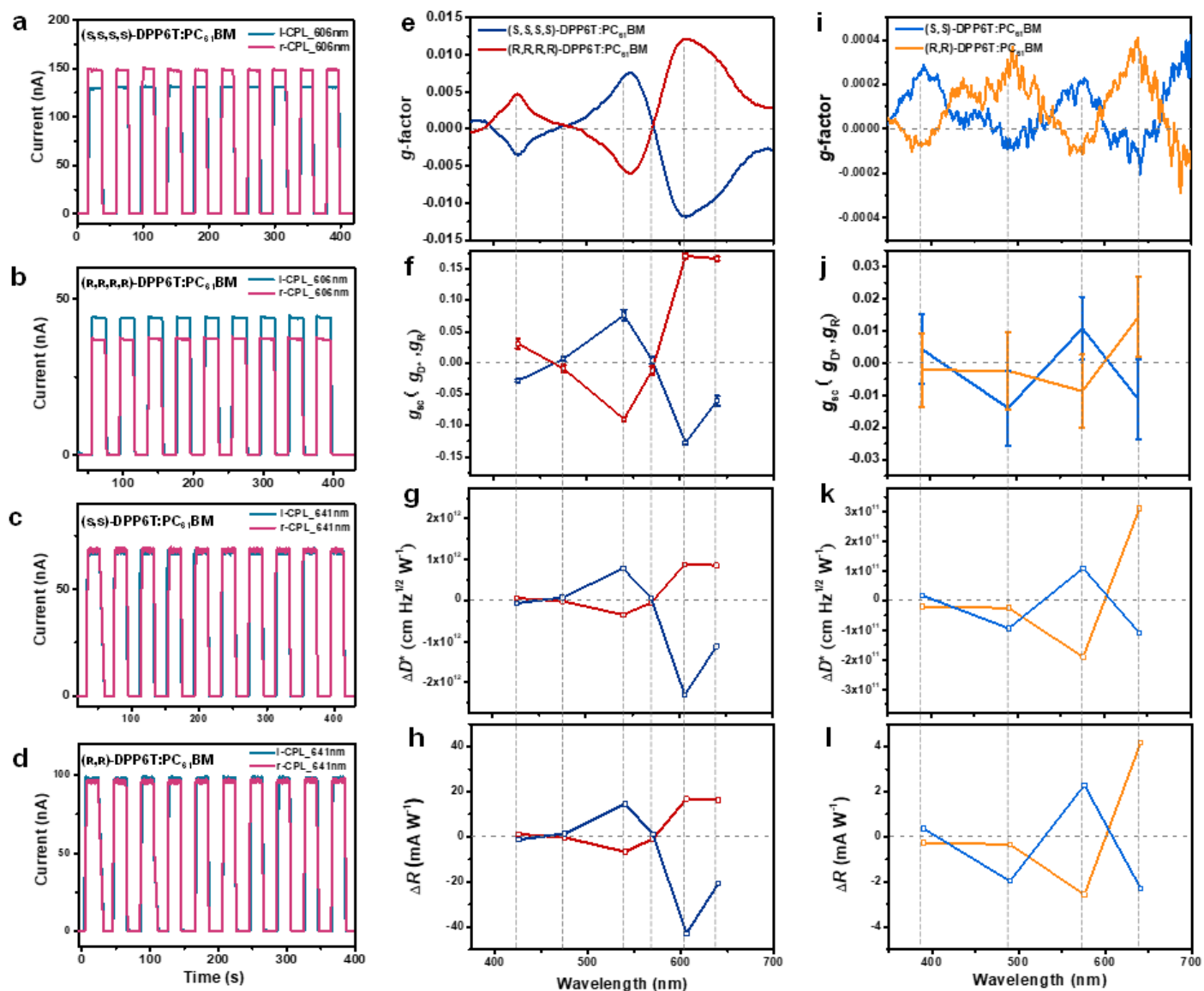


Figure 3

Direct detection of circularly polarized light by chiral OSCs. a, b, c, and d I–T switching characteristics of chiral OSCs based on (s,s,s,s)-, (R,R,R,R)-, (s,s)- and (R,R)-DPP6T:PC₆₁BM blends. The chiral OSCs were alternatively illuminated under I-CPL or r-CPL with a turn on and off cycle period of 40 s. e, f, g and h The g-factor, g_{sc} (g_R, g_D^*), ΔR and ΔD^* (the relative differences in R and D^* upon the alternating irradiation of I- and r-CPL) at CD maxima and minima for the (s,s,s,s)- and (R,R,R,R)-DPP6T:PC₆₁BM-based OSCs. i, j, k and l The g-factor, g_{sc} (g_R, g_D^*), ΔR and ΔD^* (the relative differences in R and D^* upon alternating irradiation of I- and r-CPL) at CD maxima and minima for the (s,s)- and (R,R)-DPP6T:PC₆₁BM-based OSCs.

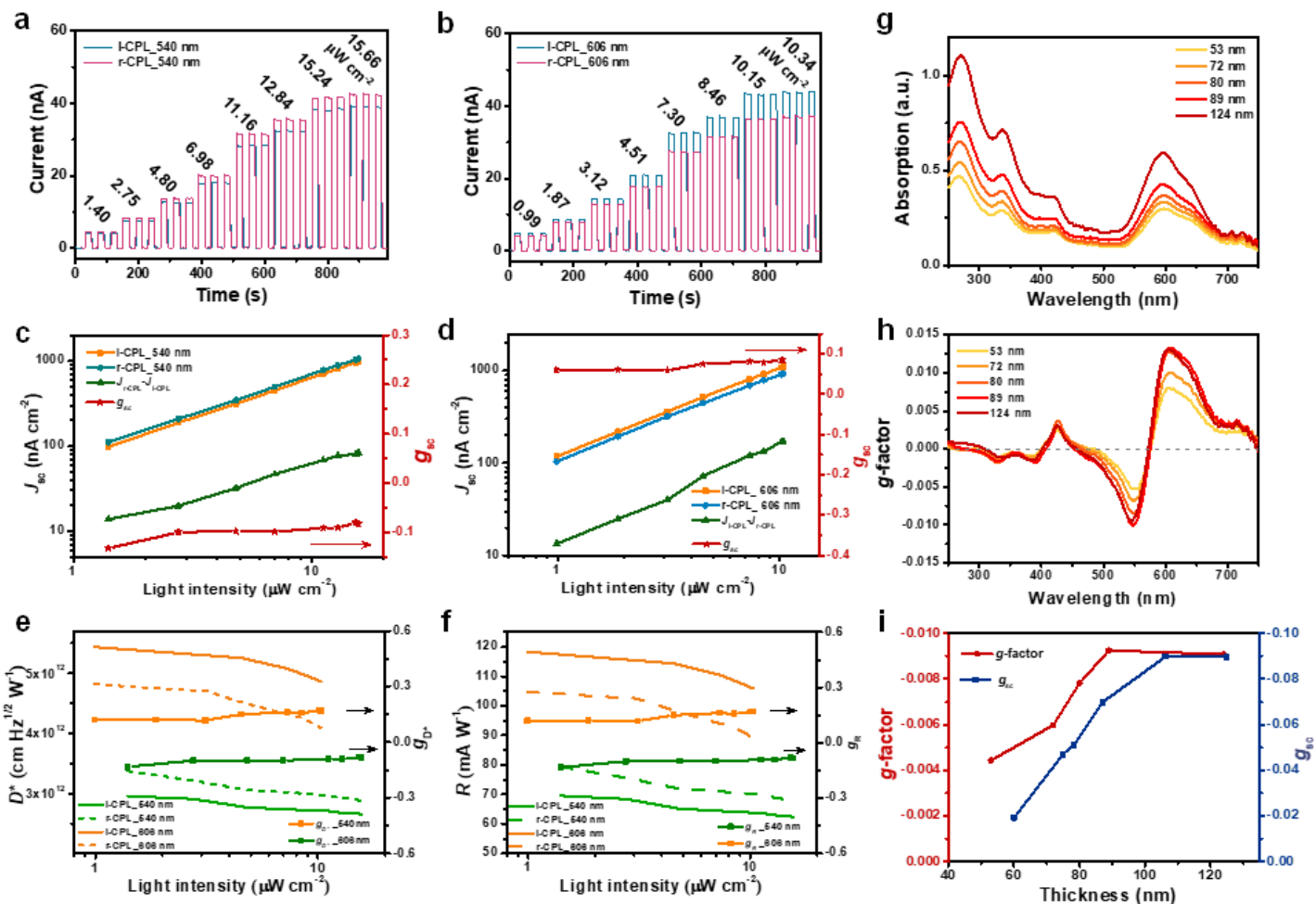


Figure 4

Influence of CPL intensity and the thickness of active layers on CPL detection sensitivity. a, b Dependence of photocurrent intensity on the incident CPL intensity at 540 and 606 nm based on (DPP6T:PC61BM) OSCs. c, d Dependence of the difference in J_{sc} upon the alternating irradiation of l- and r-CPL on the incident CPL intensity at 540 and 606 nm based on (DPP6T:PC61BM) OSCs. e, f Influence of incident l- and r-CPL intensity on D^* , R , gD^* and gR at 540 and 606 nm based on (DPP6T:PC61BM) OSCs. g Dependence of UV-vis absorption on the thickness of (DPP6T:PC61BM) blended films. h Dependence of g -factor on the thickness of (DPP6T:PC61BM) blended films. i Influence of the thickness of (DPP6T:PC61BM) blended films on g -factor and g_{sc} illuminated under 540 nm CPL.

Supplementary Files

This is a list of supplementary files associated with this preprint. Click to download.

- [LiuLXYangYCPLdetectionbyDPP6TOSCsi20200620Plain.docx](#)